Medical Physics, (2014), 41 (1), 12 p.
DOI: http://dx.doi.org/10.1118/1.4837220

Modification of the TASMIP x-ray spectral model for the simulation of microfocus x-ray sources

A. Sisniega
Departamento de Bioingeniería e Ingeniería Aeroespacial, Universidad Carlos III de Madrid, Madrid ES28911, Spain and Instituto de Investigación Sanitaria Gregorio Marañón, Madrid ES28007, Spain

M. Desco
Departamento de Bioingeniería e Ingeniería Aeroespacial, Universidad Carlos III de Madrid, Madrid ES28911, Spain; Instituto de Investigación Sanitaria Gregorio Marañón, Madrid ES28007, Spain; and Centro de Investigación Biomédica en Red de Salud Mental (CIBERSAM), Madrid ES28029, Spain

J. J. Vaquero[a)]
Departamento de Bioingeniería e Ingeniería Aeroespacial, Universidad Carlos III de Madrid, Madrid ES28911, Spain and Instituto de Investigación Sanitaria Gregorio Marañón, Madrid ES28007, Spain

Purpose: The availability of accurate and simple models for the estimation of x-ray spectra is of great importance for system simulation, optimization, or inclusion of photon energy information into data processing. There is a variety of publicly available tools for estimation of x-ray spectra in radiology and mammography. However, most of these models cannot be used directly for modeling microfocus x-ray sources due to differences in inherent filtration, energy range and/or anode material. For this reason the authors propose in this work a new model for the simulation of microfocus spectra based on existing models for mammography and radiology, modified to compensate for the effects of inherent filtration and energy range.
Methods: The authors used the radiology and mammography versions of an existing empirical model [tungsten anode spectral model interpolating polynomials (TASMIP)] as the basis of the microfocus model. First, the authors estimated the inherent filtration included in the radiology model by compar-ing the shape of the spectra with spectra from the mammography model. Afterwards, the authors built a unified spectra dataset by combining both models and, finally, they estimated the parameters of the new version of TASMIP for microfocus sources by calibrating against experimental exposure data from a microfocus x-ray source. The model was validated by comparing estimated and experimental exposure and attenuation data for different attenuating materials and x-ray beam peak energy values, using two different x-ray tubes.
Results: Inherent filtration for the radiology spectra from TASMIP was found to be equivalent to 1.68 mm Al, as compared to spectra obtained from the mammography model. To match the experi-mentally measured exposure data the combined dataset required to apply a negative filtration of about 0.21 mm Al and an anode roughness of 0.003 mm W. The validation of the model against real ac-quired data showed errors in exposure and attenuation in line with those reported for other models for radiology or mammography.
Conclusions: A new version of the TASMIP model for the estimation of x-ray spectra in micro-focus x-ray sources has been developed and validated experimentally. Similarly to other versions of TASMIP, the estimation of spectra is very simple, involving only the evaluation of polynomial expres-sions.

Key words: x-ray spectra, computer simulation, radiation dose, micro-CT, breast imaging, microfocus source

1. INTRODUCTION

The ability to obtain accurate estimations of the x-ray spectrum for a given voltage and added filtration is of great importance for the simulation and optimization of x-ray imaging systems.[1–6]

A variety of methods have been proposed for simulating x-ray spectra, especially for sources based on tungsten anodes. Spectrum simulation methods are based on various strategies for estimating the parameters of the spectrum and can be divided into three different categories: empirical methods, semiempirical methods, and realistic Monte Carlo simulation methods.

Empirical methods are based on fitting a parametric model to measured data. Examples of such methods are those that estimate the shape of the spectrum from attenuation measurements. This method uses a variety of approaches, such as the Laplace transform,[7] analytical models,[8] maximum likelihood estimations,[9] or a combination of analytical models and iterative optimization.[10] A well-known method in this family, named "tungsten anode spectral model interpolating polynomials" (TASMIP),[11, 12] models the shape of the spectrum as

[a)] Author to whom correspondence should be addressed. Electronic mail: juanjose.vaquero@uc3m.es

a function of x-ray source voltage using a set of polynomial curves fitted to experimentally measured spectra.

Semiempirical approaches make use of physical models somewhat modified or completed by measured data. Among these methods we found the earliest attempt to model *bremsstrahlung* intensity, developed by Kramers[13] and other models built upon this one, such as the one proposed by Birch and Marshall[14] and its evolution by Tucker *et al.*[15,16] Poludniowski[17] reported a procedure for the simulation of x-ray spectra based on physical models that try to describe the process of x-ray generation in metal targets more accurately than previous semiempirical attempts.

The third category of x-ray spectra generation models relies on the simulation of the x-ray generation process, by tracking the emitted electrons in the target using Monte Carlo techniques. Examples of this kind of methods were presented by Ay[18] and Bhat.[19] While Monte Carlo simulation has the potential to accurately describe the x-ray generation process and create very accurate spectra, it also implies a large computational burden that may hamper their use in applications where a large number of datasets is required.

Among all the aforementioned spectra simulation methods, TASMIP is one of the most widely used[20–25] due to its accuracy, simplicity, and public availability as part of a software package called Spektr.[26] Spektr provides extended functionalities for the generation of realistic x-ray spectra and derived variables, such as photon fluence or exposure. However, the TASMIP model used in Spektr generates x-ray spectra for typical x-ray sources used in radiology and mammography, but it lacks a dataset for the generation of spectra for general purpose microfocus x-ray sources.

Microfocus sources present a low inherent filtration, similar to that of mammography x-ray sources, but a much larger x-ray voltage span, comparable to that of radiology x-ray sources. For this reason we hypothesized that the spectra generated by microfocus x-ray sources with tungsten anode differ from the TASMIP models only in the amount of inherent filtration, and possibly in the amount of anode roughness.

Our work was motivated by the lack of simple models for the simulation of x-ray spectra generated by tungsten anode microfocus x-ray sources. We present an extension of the TASMIP empirical model for the simulation of x-ray spectra from microfocus x-ray sources.

To take advantage of the similarities between the mammography model and microfocus sources (inherent filtration) and between the radiology model and microfocus sources (voltage range) we built a new spectra dataset combining both models. To this end, we first estimated the inherent filtration included in the radiology model and removed its effect by inversely applying the Beer-Lambert's law. Thus, the low energy part of the spectra in the new dataset mostly derives from the mammography model, while the high energy part comes from the modified radiology model.

This new dataset was fine-tuned by further adjusting values of inherent filtration and anode roughness (increased inherent filtration from nonuniformities on the anode surface) with real data from experimental measurements of exposure and attenuation. With the final dataset we generated a new complete set of polynomial coefficients analogous to those already used by the TASMIP radiology and mammography models.

2. MATERIALS AND METHODS

2.A. TASMIP model for the generation of x-ray spectra

In this section we present a brief introduction to TASMIP, an empirical model proposed by Boone *et al.* for x-ray sources with tungsten anode for radiology[12] and mammography.[11]

The model is based on using polynomials to estimate the photon output in any x-ray energy bin as a function of the x-ray source voltage. The coefficients of the polynomials are obtained by fitting experimentally measured spectra to the highest order polynomial (maximum order of 3) that best represents the data points for each energy bin. Thus, the photon output for the ith energy bin—with energy E_i—can be expressed as

$$q(E_i) = a_{i0} + a_{i1} \cdot kV + a_{i2} \cdot kV^2 + a_{i3} \cdot kV^3, \quad (1)$$

where a_{in} is the n-order coefficient of the polynomial for the ith energy bin and kV is the x-ray source voltage.

The dataset used as reference for the radiology spectra was published by Fewell *et al.*,[27] and the one used for mammography was specifically measured to build the TASMIP model. The main differences between the x-ray sources used for both models were the inherent filtration of the source and the usable voltage range. The model for radiology is defined for voltages between 30 kV and 140 kV in 1 keV energy bins whereas the model for mammography is defined for voltages between 18 kV and 40 kV in 0.5 keV energy bins.

Figure 1 shows an example of spectra generated using TASMIP for mammography and radiology. The lack of similarity between spectra is evident, especially at low energies, where the spectrum is more affected by inherent filtration.

For the simulation of spectra throughout this work we used the publicly available Spektr[26] implementation of the TASMIP model. For the generation of the mammography spectra we included a new function in Spektr to read the polynomial coefficients for mammography and rearrange them into a grid with 1 keV bins.

2.B. Exposure measurements

To measure exposure in air we made use of an in-house developed cone beam micro-CT (CBμCT) scanner. The x-ray source of the system was a tungsten anode-based microfocus source, model L9631-MOD2 (Hamamatsu Photonics K.K., Hamamatsu, Japan). The available voltage range for the source was 30–110 kV with a maximum delivered power of 50 W. The electron beam of the tube hits the tungsten target at an angle of 45° (as reported by the manufacturer) and the only nominal inherent filtration in the source was a 0.5 mm-thick beryllium output window, placed at a distance of 16.8 mm of the tube focus.

We measured exposure at the isocenter of the scanner—placed at a distance of 155 mm measured from the focal spot of the source—using an Accu-Gold multi-purpose meter (Radcal, Monrovia, CA) and a 10 cm-long

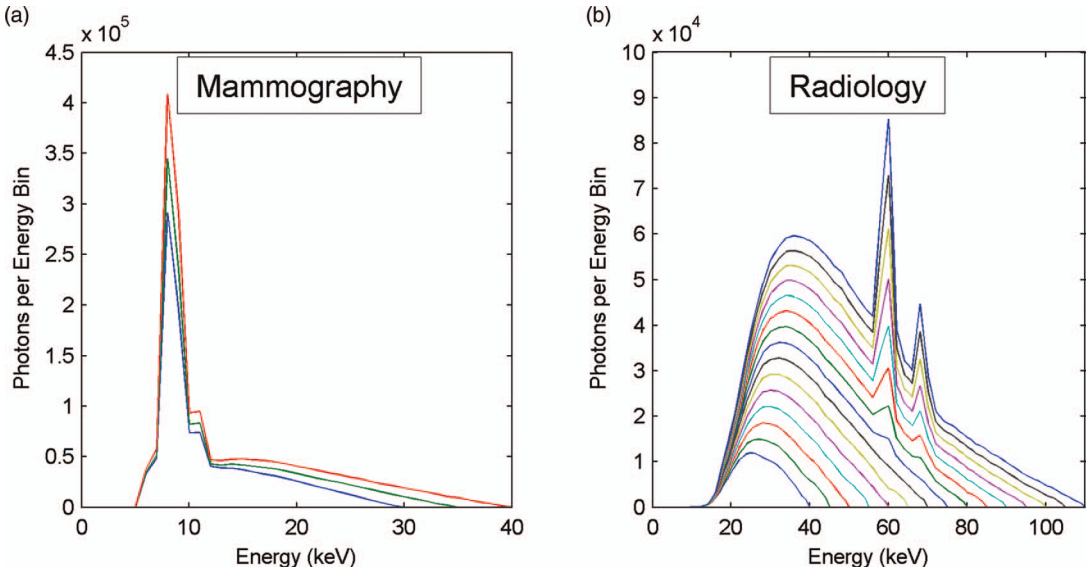

FIG. 1. Spectra generated by the TASMIP model for mammography (a) and radiology (b) x-ray sources.

pencil-shaped ion chamber (Radcal 10×6-3CT). To avoid the contamination of measurements by scattered radiation generated by the bed, the bottom edge of the ion chamber was fixed to the carbon-fiber sample holder at its very beginning in such a way that the active volume of the ion chamber was totally suspended in the air. All the measurements were translated to a distance of 1 m by applying the inverse squared distance law. The x-ray beam was collimated to a cone angle of 40° to guarantee that the beam completely covered the ion chamber.

To obtain absolute values as well as attenuation measurements as a function of x-ray source voltage we measured air exposure behind different attenuating materials. We carried out three different experiments, one to acquire data for the modification of the TASMIP model and two for the validation of the beam spectra simulated using the modified model.

In all the experiments exposure data were measured for x-ray source voltages between 30 and 110 kV in 5 kV increments, for an anode current of 0.4 mA, and with the beam attenuated by different materials and thicknesses. In the first experiment we acquired 9 datasets with the beam attenuated by aluminum of thickness 0, 0.5, 1.0, 1.5, 2.0, 2.5, 3.0, 3.5, and 4.0 mm. Incremental thickness values were obtained by stacking individual plates of aluminum with a thickness of 0.5 mm, as shown in Fig. 2(a). Aluminum plates were taken from a HVL attenuator set, model 115 A (Gammex, Middleton, WI), and had a 99% purity.

In the second experiment we also measured exposure at the same tube settings but attenuating the beam with copper plates. Copper thickness was varied between 0 and 0.3 mm by stacking 0.1 mm-thick copper plates, as depicted in Fig. 2(b). Copper plates were taken from a pure copper HVL attenuator set, model 116 (Gammex, Middleton, WI).

In the third experiment we attenuated the beam using three different thicknesses of PMMA, namely 8, 16, and 24 mm; obtained from stacking individual 8 mm-thick PMMA plates. The reference beam—i.e., the "nonattenuated" beam—contained 0.5 mm Al added filtration to mimic the minimum filtration used in realistic imaging environments. The aluminum filter was placed behind the PMMA plates to absorb most of their low-energy scattered photons and to prevent scattered radiation from reaching the ionization chamber. The arrangement for the third experiment is shown in Fig. 2(c).

To further assess the validity of the model we performed a fourth experiment using a second microfocus x-ray source from an Argus PET/CT scanner (Sedecal, Madrid, Spain).[28] The x-ray source in the Argus PET/CT is a tungsten anode microfocus source, model Apogee 5011 (Oxford Instruments, Oxfordshire, UK) with a maximum voltage of 50 kV and maximum power of 50 W. The target angle of the tube is 12° and it contains a 0.125 mm-thick beryllium output window placed at 25.6 mm from the focus. The beam is filtered with 1 mm Al.

We measured exposure in air for voltages between 30 and 50 kV in 5 kV steps, at an anode current of 0.4 mA, and with the beam attenuated by only a 1 mm Al filter. The ion chamber was placed at the isocenter of the scanner, after removing a protective PMMA tube that prevents accidental fluid leakage from the animal bed. In this case, the maximum cone angle was of 23°, covering 90% of the volume of the ion chamber. We normalized the values by a factor of 0.9 prior to compare the measurements.

2.C. Estimation of the inherent filtration and generation of the polynomial coefficients

Our hypothesis was that the differences between tungsten spectra generated by the TASMIP radiology model, the TASMIP mammography model, and microfocus x-ray sources would be only due to differences in inherent filtration plus anode roughness and/or angle. To verify this hypothesis we followed a three-step fitting process to estimate microfocus spectra from the TASMIP models and exposure data. The new microfocus spectra were used to obtain a new set of

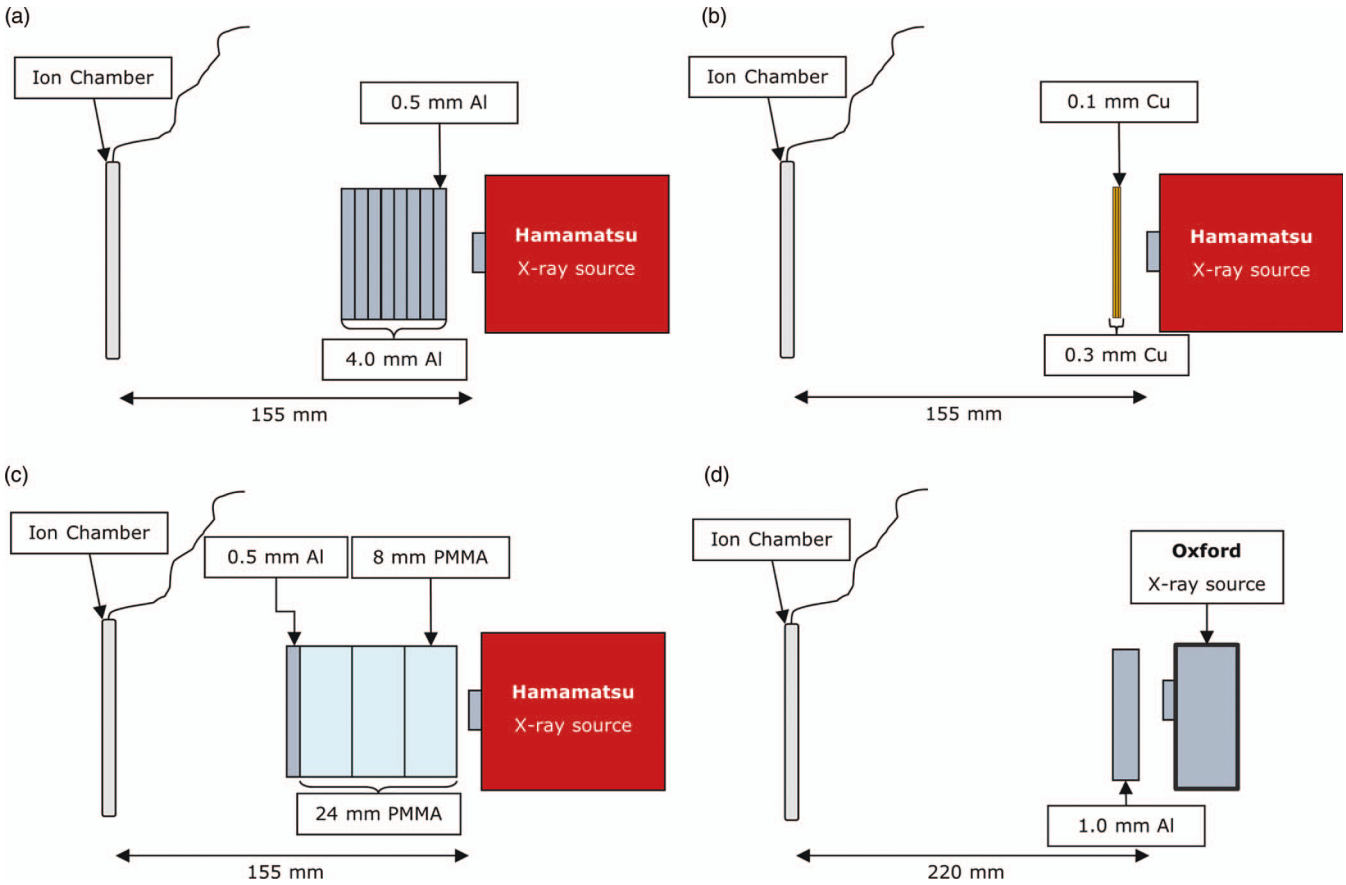

FIG. 2. Scheme of the experimental setup for the four experiments. Panels (a)–(c) show the three experiments for the Hamamatsu source at their final situation, when all the attenuating plates have been stacked and the beam is undergoing maximum attenuation. Panel (d) shows the complementary experiment carried out using an Oxford x-ray source.

polynomials as a function of x-ray source voltage. The process is graphically outlined in Fig. 3.

2.C.1. Step 1: Matching of the radiology and mammography TASMIPs

The first step of the process was aimed at finding the best match between the spectra generated by the TASMIP model for mammography and those generated by the radiology model, by estimating the aluminum and tungsten filtration in the radiology spectra and a scale factor due to the different units used in each model. To this end, we defined a three-parameter model to transform the mammography spectra and found the optimal values for the three parameters by minimizing, in the least-squares sense, the difference between the shape of the transformed mammography spectra and the one of the radiology spectra. The transformation applied to the mammography spectrum to convert it into the radiology spectrum was

$$\hat{q}_R(E) = s \cdot q_M(E) e^{-(\mu_{Al}(E)x_{Al} + \mu_W(E)x_W)}, \quad (2)$$

where E represents the energy bin, q_M is the original mammography spectrum, μ_{Al} and μ_W are the x-ray attenuation factors of aluminum and tungsten, respectively, and the unknown parameters to obtain by the minimization process are s (scale factor) and x_{Al} and x_W (thicknesses of aluminum and tungsten filter). Equation (2) actually represents mathematically our hypothesis about the origin of the differences between spectra, explained above.

The cost-function for the minimization was built by adding the squared differences between the estimated ($\hat{q}_R$) and original (q_R) radiology spectrum for each energy bin and kV value.

For the optimization process we generated a set of mammography and radiology spectra from 30 to 40 kV in 1 kV increments, since this is the range of tube potential overlap between the two models. To match the energy grid for the two spectra datasets, the mammography dataset was rebinned from its original 0.5 keV grid (see Sec. 2.A) to a grid with bins of 1 keV. Due to the lack of spectral data for energy bins below 10 keV (and to the low accuracy of the first bins) in the radiology dataset, we restricted the fitting to energies above 15 keV.

Optimal parameters of the model (s, x_{Al}, and x_W) were found by minimizing the cost-function using the Levenberg-Marquardt method as implemented in the *lsqnonlin* function of the Matlab® (Mathworks, MA) package.

2.C.2. Step 2: Generation of a combined spectra dataset

The second step of the process involved the generation of a new set of x-ray spectra ($\hat{q}_c$) by combining the mammography

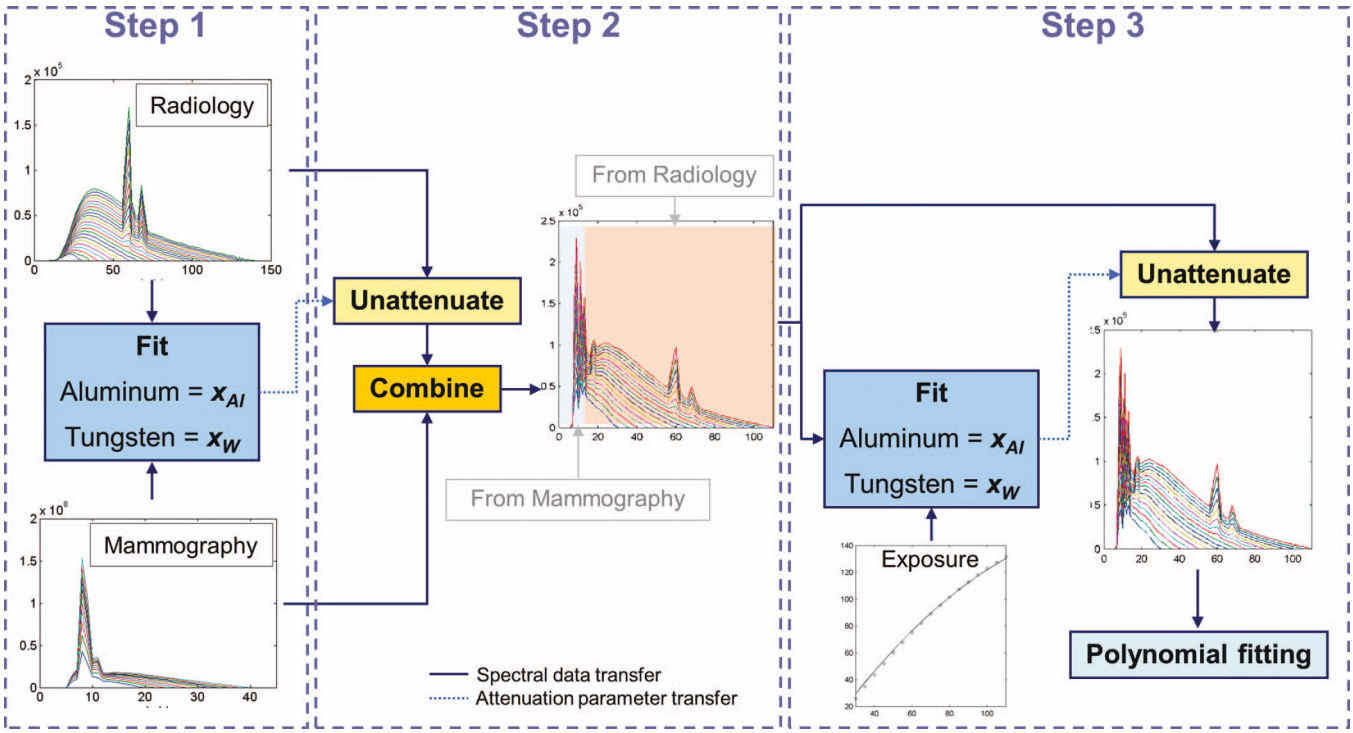

FIG. 3. Outline of the method followed for obtaining the polynomial coefficients for the new version of the TASMIP model for microfocus sources. Solid dark-blue arrows represent transferring spectral data while dashed light-blue arrows denote transferring aluminum and tungsten thickness resulting from the fitting process.

and radiology datasets over the whole voltage span. The new data were obtained as follows.

First, a new set of radiology spectra was simulated for voltages between 30 and 110 kV in 5 kV steps. The effects of inherent filtration were removed by inversely applying the Beer's law using the negative values of the estimated thickness of aluminum (x_{Al}) and tungsten (x_W). This procedure actually implements a spectral "unattenuation."

As stated above, low energy values in the radiology model are not valid. For this reason we used the mammography model for the low energy part of the spectra. Data from Boone *et al.*[11] showed a large degree of linearity for the first energy bins of the mammographic model. For this reason we removed the higher order terms of the original polynomial coefficients and linearly extrapolated the values of energy bins from 6 to 13 keV beyond the voltage range covered by the mammographic model and up to 110 kVp, matching the kVp values used to generate the radiology dataset. Values up to 13 keV in the "unattenuated" radiology spectra were substituted by the extrapolation of mammography data, thus covering the complete voltage range of the microfocus x-ray source used in the present work.

2.C.3. Step 3: Generation of the microfocus TASMIP model

In this step, the dataset coming from the previous stage was modified to match experimental measurements by minimizing (in the least-squares sense) the difference between estimated and measured attenuation values for the aluminum plates (see Sec. 2.B). Attenuation was calculated as the ratio of exposures for the attenuated and nonattenuated beams. We followed a method similar to that proposed by Meghzifene *et al.*[29] who made use of attenuation measurements to estimate the inherent filtration of the source by means of numerical optimization.

We obtained the exposure for the simulated spectra by integrating, across energy, the inverse of the x-ray quanta per unit of exposure, weighted by the spectra in the dataset. The number of x-ray quanta per unit exposure for a particular energy bin can be obtained using the expression by Johns:[30]

$$\frac{\Phi}{X} = \frac{5.43 \times 10^5}{(\mu(E)/\rho)_{en}\, E}, \tag{3}$$

where $(\mu(E)/\rho)_{en}$ is the mass-energy absorption coefficient for air, X is the exposure value in mR, and Φ is the photon fluence in photons/mm^2. Using Eq. (3), the total exposure value is given by[12]

$$X_t = \int_0^{E_{\max}} \frac{X}{\Phi}(E)\hat{q}_u(E)dE, \tag{4}$$

where $\hat{q}_u$ is the estimated microfocus spectrum. The value of $\hat{q}_u$ was estimated by finding the aluminum and tungsten filtration that, when applied to $\hat{q}_c$, minimized the difference between estimated and measured attenuation. Analogously to Eq. (2), $\hat{q}_u$ is given by

$$\hat{q}_u(E) = \hat{q}_c(E)e^{-(\mu_{Al}(E)x_{Al}+\mu_W(E)x_W)}. \tag{5}$$

We built the last fitting process based on two premises: first, that the housing of x-ray sources—responsible for inherent filtration—contains several materials that are not exactly aluminum and, therefore, the equivalent aluminum thickness could vary with x-ray source voltage; and, second, that anode roughness can be modeled as a voltage-independent tungsten thickness.[31] For these reasons we set as parameters for the optimization process one value of aluminum thickness per kV plus a single tungsten thickness shared for all kV values.

Attenuation data were computed for the aluminum filtered exposure data—see Sec. 2.B and Fig. 2(a)—using 0 mm Al as the reference point (i.e., we used eight attenuation points, namely 0.5, 1.0, 1.5, 2.0, 2.5, 3.0, 3.5, and 4.0 mm Al). The cost function was minimized using the Levenberg-Marquardt method.

Estimated microfocus spectra ($\hat{q}_u$) generated after the optimization process were subsequently used to find the coefficients of the new TASMIP polynomials. The polynomial fitting was done as described by Boone *et al.*,[12] finding a polynomial (with a maximum degree of 3) that related x-ray source voltage to photon output, per energy bin. We used the *polyfit* routine in Matlab® for finding the polynomial coefficients.

2.D. Evaluation of the spectral model

We evaluated the accuracy of the spectra obtained with the modified TASMIP model for microfocus sources in terms of exposure and attenuation, for the four exposure datasets described in Sec. 2.B, using two different models of x-ray tubes.

In particular, we compared the exposure estimated by the simulated spectra to the one measured behind the aluminum and PMMA attenuators, and the attenuation factors using 0.5 mm Al as the reference beam for both materials. We also compared attenuation factors in copper using 0.1 mm Cu as the reference beam.

Finally, we studied the accuracy of the model on exposure data measured with the second x-ray source (denoted Oxford from now on). To this end, we compared, as a function of voltage, the exposure measured for the Hamamatsu source, the one for the Oxford source and the exposure calculated using the simulated spectra from the microfocus TASMIP model.

The deviation between simulated and experimental data was quantified by the average relative absolute error, computed using the following expression:

$$\varepsilon = \frac{1}{N}\sum_{i=1}^{N}\frac{|\hat{x}_i - x_i|}{x_i}, \tag{6}$$

where $\hat{x}_i$ is the simulated quantity, x_i is the measured quantity, and N is the number of data points.

3. RESULTS

The new set of coefficients for the polynomial curves of the modified TASMIP model can be found in the Appendix.

Figure 4 shows a set of spectra generated using the modified TASMIP for microfocus sources, with no added filtration.

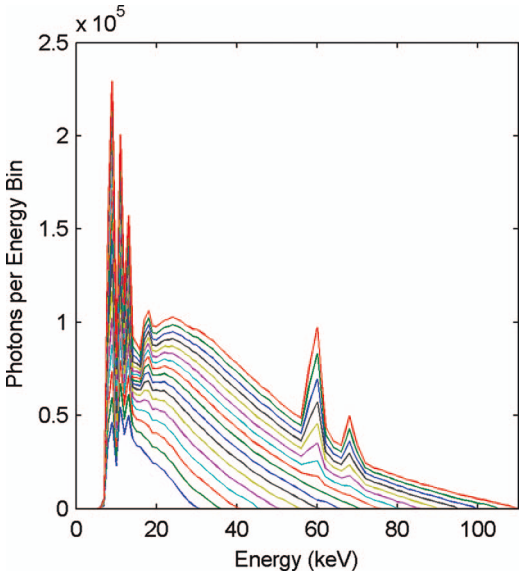

FIG. 4. Spectra generated by the modified TASMIP model for microfocus x-ray sources, plotted for a range of voltages between 30 and 110 kV, in 5kV increments.

The spectra show a large number of photons in low energy bins, resembling the shape of the mammography spectra in that part of the energy span—see Fig. 1(a), and it follows the shape of the radiology spectra for higher energy photons, although after removing the effect of inherent filtration.

We found the radiology spectra to present an inherent filtration of $x_{Al} = 1.68$ mm Al with a negligible quantity of tungsten filtration ($x_W < 10^{-10}$ mm). The second fitting process, which matched attenuation and exposure measurements to the spectra resulting from the combination of mammography and radiology data, yielded a negative value of aluminum thickness for all the voltages, ranging between -0.20 and -0.22 mm Al and a value of tungsten filtration of 0.0029 mm W, which corresponds to a value of roughness of the anode of $\sim 3\ \mu$m.[31]

Figure 5(a) presents exposure as a function of source voltage for the raw beam (i.e., 0 mm Al added filtration). Simulated values show a good agreement with measured exposure, with an average relative error of 0.03. The exposure curve for the beam filtered by different thicknesses of aluminum is shown in Fig. 5(b). In this case the simulated data also show a good agreement with measured exposure.

Simulated attenuation values for aluminum—see Fig. 6(a)—showed very good agreement with measured data with a maximum average error of 0.08, for a peak energy of 35 kV. For the case of copper, the correspondence between simulated and measured attenuation is worse, with a deviation that can be visually appreciated in Fig. 6(b). The maximum average error in this case was of 0.15, for the data corresponding to 45 kV. Copper data for x-ray source voltages below 40 kV could not be evaluated due to the insufficient signal for large thickness values.

To illustrate the difference between the modified model and the original TASMIP for radiological sources, in Fig. 7 we compare simulated attenuation for the classic TASMIP (black

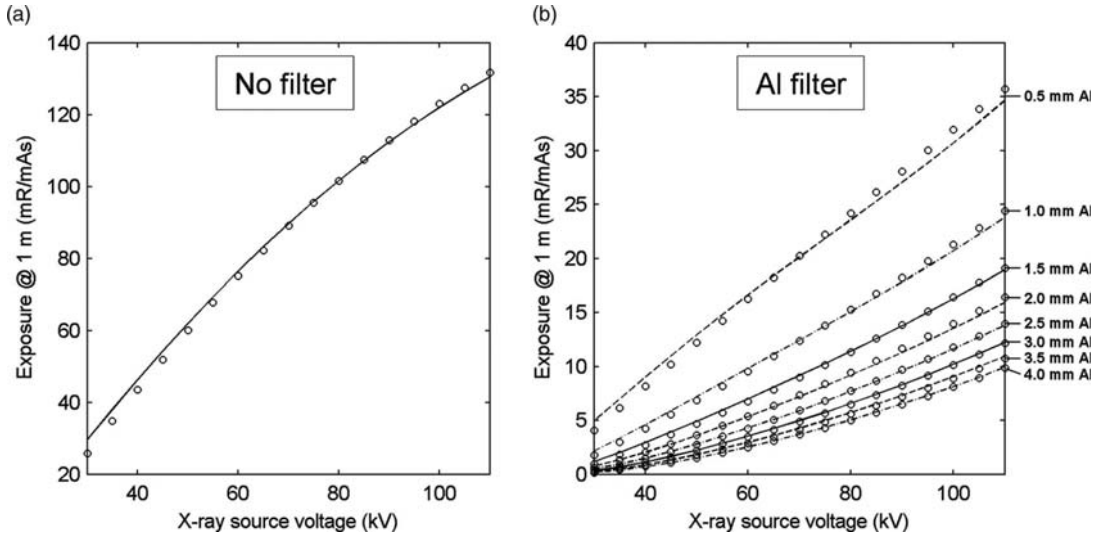

FIG. 5. Panel (a) shows exposure at 1 m from the source, measured (circular markers) and estimated (lines), using the model with no added beam filtration. The x-ray source voltage in panel (a) ranged from 30 to 110 kV in 5 kV increments. Exposure measurements and estimations for a beam filtered by aluminum are compared in panel (b), for a range of added filtration between 0.5 and 4 mm Al in 0.5 mm increments.

curves) with measured data (gray curves). The deviation is larger in this case and it is especially noticeable for copper, with average relative errors between 0.6 and 4.4.

Simulated exposure and attenuation for the PMMA slabs is shown in Fig. 8, together with measured data. Simulated and measured curves present small deviations, with a maximum relative average error of 0.05 in exposure (for 8 mm PMMA) and of 0.06 in attenuation (for 24 mm PMMA).

The errors for the different attenuating materials for the range of voltages contemplated in the study are shown in Table I.

The simulated exposure for 1 mm Al added filtration agreed to a great extent with the data measured for the Hamamatsu x-ray source (already shown in Fig. 5(b) and depicted again in Fig. 9) and for the Oxford x-ray source, shown in Fig. 9. The last point in the exposure curve for the Oxford source broke the trend and departed not only from the simulated data but also from the experimental data obtained with the Hamamatsu source.

4. DISCUSSION AND CONCLUSIONS

In this work we present the extension of the TASMIP models to enable their use for tungsten anode microfocus x-ray sources. We modified the models by calculating the inherent filtration included in the original model for radiology as compared to the model for mammography, which only included the output beryllium window of the tube. After

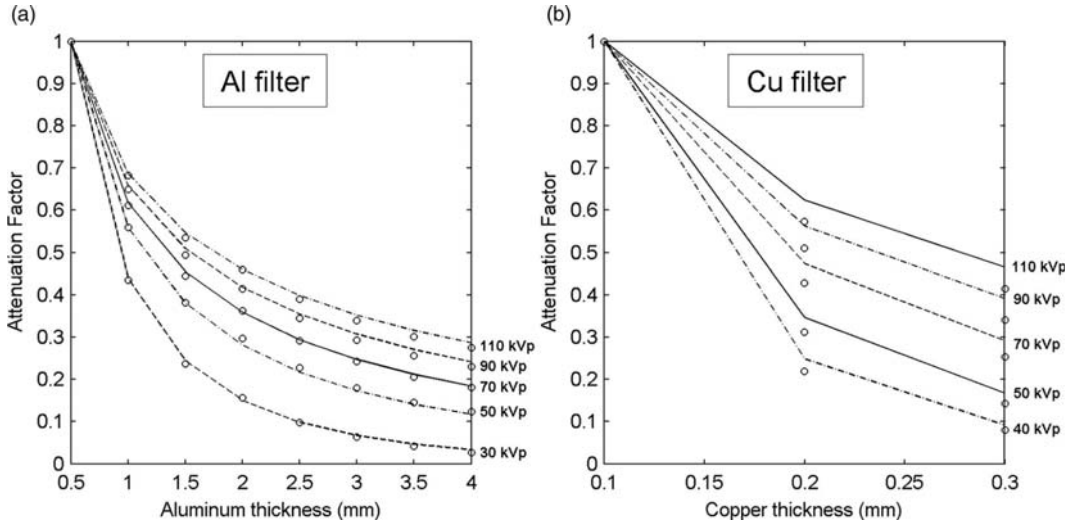

FIG. 6. Attenuation curves from measured (circular markers) and estimated (lines) data as a function of added filtration for different x-ray source voltages. Panel (a) shows the attenuation values for different thickness of aluminum referred to 0.5 mm Al. Attenuation values using copper as attenuating material are shown in panel (b), using 0.1 mm Cu as the reference point.

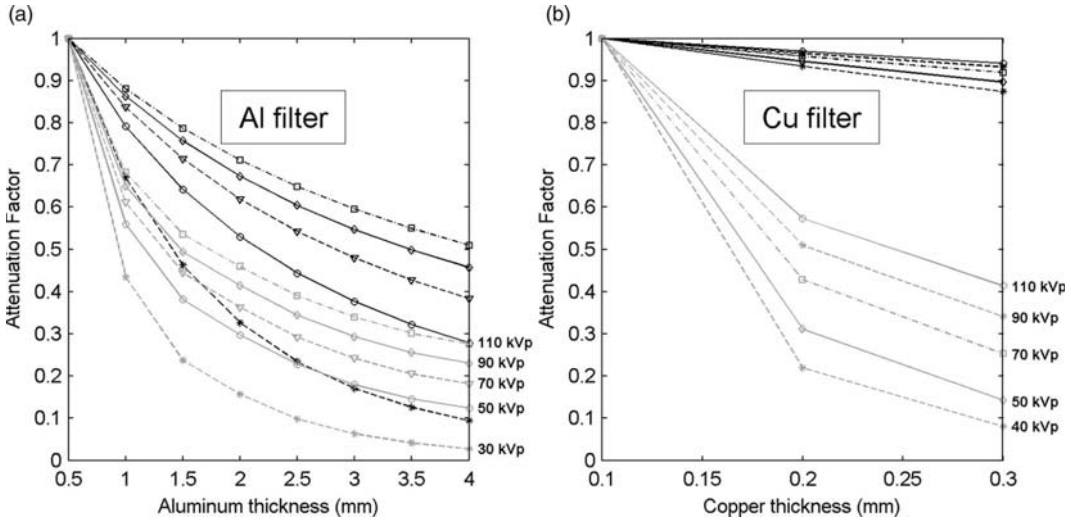

FIG. 7. Comparison between attenuation values for aluminum (a) and for copper (b) attenuators obtained by the classic radiological version of the TASMIP model (black curves) and experimentally determined (gray curves).

finding the value of inherent filtration that accounts for the difference between the radiology and mammography datasets we could build a complete dataset by combining them. Then we found accurate values of inherent filtration and anode roughness for this new dataset using experimental attenuation values, with an approach similar to the one presented in Ref. 29.

The estimated value of differential inherent filtration between the radiology and mammography datasets was found to be of 1.68 mm Al, in line with the value of inherent filtration reported by Boone *et al.*, who obtained a value of ∼2.0 mm Al for the Fewell spectra, computed as the nominal 1.1 mm Al plus an extra filtration of ∼0.88 mm (for voltages between 30 and 40 kV) which was necessary to match measured attenuation.[12]

We found that experimental data for our microfocus x-ray source better matched a value of inherent filtration of ∼1.5 mm Al, with an extra filtration of ∼3 μm W. This extra filtration from tungsten could arise from roughness in the anodes used in Refs. 11 and 12, and falls in the range of values reported by Nowotny and Meghzifene,[31] who found anode roughness ranging from 0 to 6 μm for a set of six anodes extracted from used x-ray sources.

Errors shown by our new model are in line with errors reported by Ay *et al.*[32] for other spectrum simulation models in the radiology range, with ∼1.2 mm Al inherent filtration. For attenuation curves for aluminum thicknesses ranging from 0 to 25 mm and for 100 kVp, they reported a mean error of 10.4% (0.104 relative error) for the IPEM model,[33] 9.9% for the model by Birch and Marshall,[14] 4.5% for the

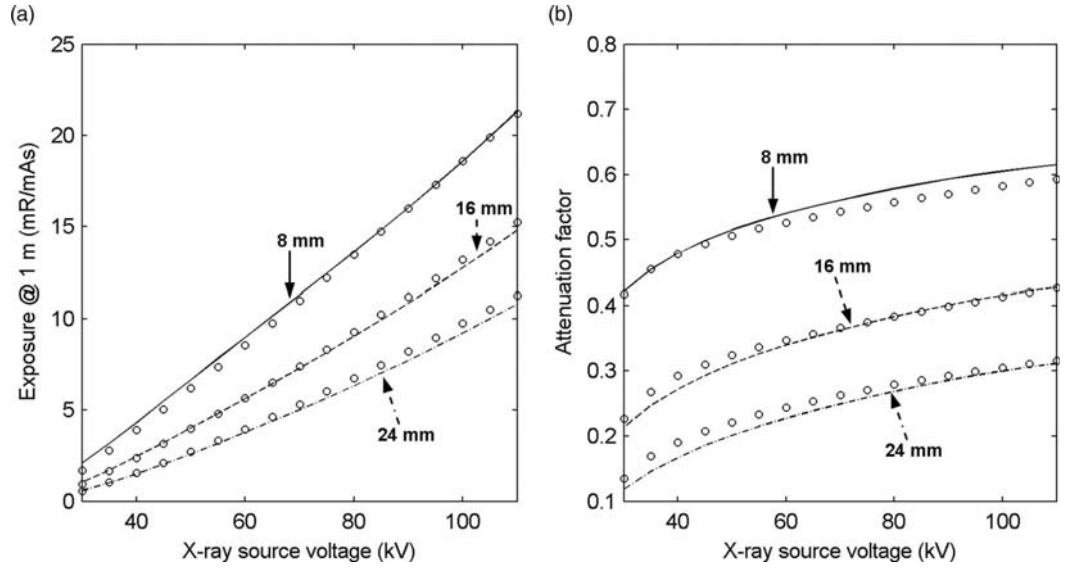

FIG. 8. Exposure (a) and attenuation values (b) measured (circular markers) and estimated (curves) using the modified TASMIP model behind PMMA plates of different thicknesses, as a function of x-ray source voltage. We used 0.5 mm Al added filtration for the reference—i.e., nonattenuated—beam.

TABLE I. Average relative error (ε) in simulated attenuation data, as a function of x-ray source voltage.

	X-ray source voltage								
Material	30 kV	40 kV	50 kV	60 kV	70 kV	80 kV	90 kV	100 kV	110 kV
Al	0.07	0.08	0.03	0.01	0.02	0.03	0.03	0.03	0.02
Cu	N/A	0.14	0.14	0.14	0.13	0.13	0.13	0.12	0.10
PMMA	0.06	0.07	0.05	0.04	0.03	0.02	0.02	0.02	0.02

model by Tucker *et al.*,[15] 0.6% for the TASMIP radiology model,[12] 3.0% for a Monte Carlo model using the MCNP package,[18] and 7.7% for a Monte Carlo model based on the EGS4 package.[19] These values are in line with the mean error of 3.3% for aluminum thicknesses up to 4 mm shown by our modified TASMIP model and with a mean error of 11.7% when using copper with a maximum thickness of 0.3 mm. While in our validation study the maximum thickness of aluminum is lower than in the study by Ay,[32] the maximum attenuation factor is similar (∼0.05), allowing us to compare our results with those in Ref. 32.

Our model is suitable for the simulation of spectra generated by microfocus sources with tungsten anode in reflection mode, such as the two tubes used for the evaluation in this work and commonly used in small-animal imaging. However, there exists a variety of microfocus x-ray sources that incorporates anodes made of materials different from tungsten or anodes working in transmission mode[34] for which our model has not been tested. The model is not applicable to sources with nontungsten anodes given the difference in characteristic radiation and atomic number. Further work, outside the scope of this paper, would be necessary to evaluate the applicability of our model to sources based on tungsten anodes configured in transmission mode.

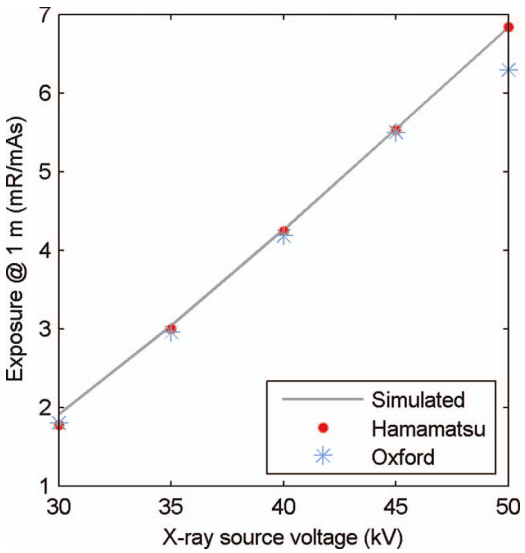

FIG. 9. Experimentally determined (markers) and simulated (curve) exposure values for x-ray beams between 30 and 50 kV and 1 mm Al filtration. Dots represent the values obtained for the Hamamatsu x-ray source and stars represent those obtained for the Oxford x-ray source.

Recent developments for high-resolution x-ray imaging also make use of microfocus sources based on the liquid-metal-jet technology.[35] In this type of sources the electron beam is directed towards a liquid metal alloy on continuous circulation. This provides much more efficient heat dissipation and allows increasing the photon flux. The metals included in the alloys have properties different from those of tungsten and, therefore, render our model not applicable for the simulation of this type of microfocus sources.

In conclusion, we have generated a new set of polynomial coefficients for the simulation of x-ray spectra for tungsten anode microfocus x-ray sources that can be used following the rationale of the TASMIP model. As in the case of the TASMIP model, the generation of spectra is very simple, involving only the evaluation of polynomial curves as a function of x-ray source voltage. The new set of polynomials can be straightforwardly included in Spektr, taking advantage of the additional features offered by this package. The results showed a good agreement with experimental data, in line with other, usually more complicated, spectral models developed for radiology or mammography.

This new model may be useful to simulate spectra for tungsten anode microfocus x-ray sources covering a large span of voltages.

ACKNOWLEDGMENTS

The authors thank John Boone, Ph. D. (University of California Davis) for fruitful discussions during the preparation of the paper. The research was supported by the Innovative Medicines Initiative Joint Undertaking under Grant Agreement No. 115337, which comprises financial contributions from the European Union's Seventh Framework Programme (FP7/2007-2013) and EFPIA companies' in kind contribution. This work was also partially funded by the AMIT project (CEN-20101014) from the CDTI-CENIT program, projects TEC2010-21619-C04-01, TEC2011-28972-C02-01, and PI11/00616 from the Spanish Ministerio de Ciencia e Innovación. A. Sisniega is funded by an FPU grant from the Spanish Ministerio de Educación.

APPENDIX: TASMIP COEFFICIENTS

This appendix reports the polynomial coefficients for the microfocus TASMIP model. Table II shows the value of the coefficients for the different energy bins.

TABLE II. Polynomial coefficients of the TASMIP model for microfocus sources.

Photon energy (keV)	a_0	a_1	a_2	a_3
6.00	$-6.39 \times 10^{+01}$	$7.01 \times 10^{+00}$	1.07×10^{-01}	-1.15×10^{-03}
7.00	$-5.98 \times 10^{+02}$	$7.02 \times 10^{+01}$	5.28×10^{-01}	-6.39×10^{-03}
8.00	$-1.02 \times 10^{+04}$	$8.95 \times 10^{+02}$	$2.61 \times 10^{+01}$	-1.87×10^{-01}
9.00	$-1.59 \times 10^{+04}$	$1.32 \times 10^{+03}$	$3.13 \times 10^{+01}$	-2.10×10^{-01}
10.00	$-1.25 \times 10^{+04}$	$1.29 \times 10^{+03}$	$-3.42 \times 10^{+00}$	-5.21×10^{-03}
11.00	$-3.47 \times 10^{+04}$	$3.34 \times 10^{+03}$	$-1.27 \times 10^{+01}$	1.63×10^{-02}
12.00	$-3.32 \times 10^{+04}$	$3.23 \times 10^{+03}$	$-2.99 \times 10^{+01}$	1.12×10^{-01}
13.00	$-4.65 \times 10^{+04}$	$4.18 \times 10^{+03}$	$-3.65 \times 10^{+01}$	1.39×10^{-01}
14.00	$-4.51 \times 10^{+04}$	$4.13 \times 10^{+03}$	$-5.25 \times 10^{+01}$	2.40×10^{-01}
15.00	$-4.47 \times 10^{+04}$	$3.77 \times 10^{+03}$	$-4.38 \times 10^{+01}$	1.87×10^{-01}
16.00	$-4.90 \times 10^{+04}$	$3.93 \times 10^{+03}$	$-4.57 \times 10^{+01}$	1.91×10^{-01}
17.00	$-4.72 \times 10^{+04}$	$3.47 \times 10^{+03}$	$-3.37 \times 10^{+01}$	1.31×10^{-01}
18.00	$-4.75 \times 10^{+04}$	$3.26 \times 10^{+03}$	$-2.85 \times 10^{+01}$	1.05×10^{-01}
19.00	$-4.94 \times 10^{+04}$	$3.25 \times 10^{+03}$	$-2.95 \times 10^{+01}$	1.10×10^{-01}
20.00	$-5.54 \times 10^{+04}$	$3.53 \times 10^{+03}$	$-3.32 \times 10^{+01}$	1.26×10^{-01}
21.00	$-5.70 \times 10^{+04}$	$3.45 \times 10^{+03}$	$-3.09 \times 10^{+01}$	1.13×10^{-01}
22.00	$-5.98 \times 10^{+04}$	$3.46 \times 10^{+03}$	$-2.99 \times 10^{+01}$	1.07×10^{-01}
23.00	$-6.05 \times 10^{+04}$	$3.32 \times 10^{+03}$	$-2.73 \times 10^{+01}$	9.58×10^{-02}
24.00	$-6.24 \times 10^{+04}$	$3.27 \times 10^{+03}$	$-2.59 \times 10^{+01}$	8.91×10^{-02}
25.00	$-6.21 \times 10^{+04}$	$3.07 \times 10^{+03}$	$-2.24 \times 10^{+01}$	7.32×10^{-02}
26.00	$-6.23 \times 10^{+04}$	$2.92 \times 10^{+03}$	$-1.96 \times 10^{+01}$	5.98×10^{-02}
27.00	$-6.28 \times 10^{+04}$	$2.78 \times 10^{+03}$	$-1.72 \times 10^{+01}$	4.78×10^{-02}
28.00	$-6.43 \times 10^{+04}$	$2.70 \times 10^{+03}$	$-1.54 \times 10^{+01}$	3.87×10^{-02}
29.00	$-6.31 \times 10^{+04}$	$2.57 \times 10^{+03}$	$-1.41 \times 10^{+01}$	3.63×10^{-02}
30.00	$-6.26 \times 10^{+04}$	$2.47 \times 10^{+03}$	$-1.30 \times 10^{+01}$	3.37×10^{-02}
31.00	$-6.27 \times 10^{+04}$	$2.43 \times 10^{+03}$	$-1.32 \times 10^{+01}$	3.74×10^{-02}
32.00	$-6.40 \times 10^{+04}$	$2.42 \times 10^{+03}$	$-1.32 \times 10^{+01}$	3.84×10^{-02}
33.00	$-6.32 \times 10^{+04}$	$2.30 \times 10^{+03}$	$-1.19 \times 10^{+01}$	3.39×10^{-02}
34.00	$-6.26 \times 10^{+04}$	$2.20 \times 10^{+03}$	$-1.06 \times 10^{+01}$	2.95×10^{-02}
35.00	$-6.36 \times 10^{+04}$	$2.17 \times 10^{+03}$	$-1.05 \times 10^{+01}$	2.92×10^{-02}
36.00	$-6.49 \times 10^{+04}$	$2.16 \times 10^{+03}$	$-1.05 \times 10^{+01}$	2.95×10^{-02}
37.00	$-6.58 \times 10^{+04}$	$2.13 \times 10^{+03}$	$-1.00 \times 10^{+01}$	2.75×10^{-02}
38.00	$-6.73 \times 10^{+04}$	$2.11 \times 10^{+03}$	$-9.81 \times 10^{+00}$	2.64×10^{-02}
39.00	$-6.64 \times 10^{+04}$	$2.04 \times 10^{+03}$	$-9.21 \times 10^{+00}$	2.49×10^{-02}
40.00	$-6.86 \times 10^{+04}$	$2.08 \times 10^{+03}$	$-1.01 \times 10^{+01}$	2.94×10^{-02}
41.00	$-6.50 \times 10^{+04}$	$1.92 \times 10^{+03}$	$-8.52 \times 10^{+00}$	2.42×10^{-02}
42.00	$-6.44 \times 10^{+04}$	$1.86 \times 10^{+03}$	$-7.71 \times 10^{+00}$	2.07×10^{-02}
43.00	$-5.58 \times 10^{+04}$	$1.45 \times 10^{+03}$	$-2.63 \times 10^{+00}$	$0.00 \times 10^{+00}$
44.00	$-5.52 \times 10^{+04}$	$1.39 \times 10^{+03}$	$-2.28 \times 10^{+00}$	$0.00 \times 10^{+00}$
45.00	$-7.24 \times 10^{+04}$	$2.02 \times 10^{+03}$	$-1.03 \times 10^{+01}$	3.23×10^{-02}
46.00	$-7.20 \times 10^{+04}$	$1.96 \times 10^{+03}$	$-9.65 \times 10^{+00}$	2.87×10^{-02}
47.00	$-6.73 \times 10^{+04}$	$1.73 \times 10^{+03}$	$-6.75 \times 10^{+00}$	1.73×10^{-02}
48.00	$-6.59 \times 10^{+04}$	$1.61 \times 10^{+03}$	$-5.33 \times 10^{+00}$	1.17×10^{-02}
49.00	$-7.36 \times 10^{+04}$	$1.88 \times 10^{+03}$	$-8.72 \times 10^{+00}$	2.47×10^{-02}
50.00	$-8.38 \times 10^{+04}$	$2.23 \times 10^{+03}$	$-1.31 \times 10^{+01}$	4.14×10^{-02}
51.00	$-7.86 \times 10^{+04}$	$2.05 \times 10^{+03}$	$-1.14 \times 10^{+01}$	3.58×10^{-02}
52.00	$-7.52 \times 10^{+04}$	$1.89 \times 10^{+03}$	$-9.75 \times 10^{+00}$	2.97×10^{-02}
53.00	$-7.78 \times 10^{+04}$	$1.96 \times 10^{+03}$	$-1.06 \times 10^{+01}$	3.29×10^{-02}
54.00	$-8.21 \times 10^{+04}$	$2.08 \times 10^{+03}$	$-1.21 \times 10^{+01}$	3.86×10^{-02}
55.00	$-9.11 \times 10^{+04}$	$2.36 \times 10^{+03}$	$-1.55 \times 10^{+01}$	5.20×10^{-02}
56.00	$-7.73 \times 10^{+04}$	$1.85 \times 10^{+03}$	$-9.80 \times 10^{+00}$	3.10×10^{-02}
57.00	$-2.90 \times 10^{+04}$	$1.22 \times 10^{+02}$	$7.78 \times 10^{+00}$	-1.25×10^{-02}
58.00	$1.65 \times 10^{+04}$	$-1.48 \times 10^{+03}$	$2.38 \times 10^{+01}$	-4.98×10^{-02}
59.00	$5.23 \times 10^{+04}$	$-2.74 \times 10^{+03}$	$3.62 \times 10^{+01}$	-7.66×10^{-02}
60.00	$8.52 \times 10^{+04}$	$-3.90 \times 10^{+03}$	$4.73 \times 10^{+01}$	-9.88×10^{-02}
61.00	$1.05 \times 10^{+04}$	$-1.31 \times 10^{+03}$	$2.12 \times 10^{+01}$	-3.92×10^{-02}
62.00	$-5.39 \times 10^{+04}$	$8.75 \times 10^{+02}$	1.62×10^{-01}	$0.00 \times 10^{+00}$
63.00	$-5.99 \times 10^{+04}$	$1.04 \times 10^{+03}$	$-1.19 \times 10^{+00}$	$0.00 \times 10^{+00}$

TABLE II. (*Continued.*)

Photon energy (keV)	a_0	a_1	a_2	a_3
64.00	$-9.64 \times 10^{+04}$	$2.29 \times 10^{+03}$	$-1.51 \times 10^{+01}$	4.80×10^{-02}
65.00	$-1.21 \times 10^{+05}$	$3.06 \times 10^{+03}$	$-2.34 \times 10^{+01}$	7.73×10^{-02}
66.00	$-1.00 \times 10^{+05}$	$2.33 \times 10^{+03}$	$-1.53 \times 10^{+01}$	4.69×10^{-02}
67.00	$-4.54 \times 10^{+04}$	$4.82 \times 10^{+02}$	$3.43 \times 10^{+00}$	-5.47×10^{-03}
68.00	$-1.18 \times 10^{+03}$	$-1.01 \times 10^{+03}$	$1.83 \times 10^{+01}$	-4.39×10^{-02}
69.00	$-4.93 \times 10^{+04}$	$5.65 \times 10^{+02}$	$2.34 \times 10^{+00}$	$0.00 \times 10^{+00}$
70.00	$-1.62 \times 10^{+05}$	$4.20 \times 10^{+03}$	$-3.57 \times 10^{+01}$	1.24×10^{-01}
71.00	$-1.28 \times 10^{+05}$	$3.11 \times 10^{+03}$	$-2.39 \times 10^{+01}$	7.82×10^{-02}
72.00	$-6.87 \times 10^{+04}$	$1.19 \times 10^{+03}$	$-3.14 \times 10^{+00}$	$0.00 \times 10^{+00}$
73.00	$-7.34 \times 10^{+04}$	$1.29 \times 10^{+03}$	$-3.74 \times 10^{+00}$	$0.00 \times 10^{+00}$
74.00	$-1.34 \times 10^{+05}$	$3.20 \times 10^{+03}$	$-2.41 \times 10^{+01}$	7.11×10^{-02}
75.00	$-1.72 \times 10^{+05}$	$4.37 \times 10^{+03}$	$-3.62 \times 10^{+01}$	1.13×10^{-01}
76.00	$-1.53 \times 10^{+05}$	$3.77 \times 10^{+03}$	$-3.00 \times 10^{+01}$	9.18×10^{-02}
77.00	$-7.88 \times 10^{+04}$	$1.35 \times 10^{+03}$	$-4.14 \times 10^{+00}$	$0.00 \times 10^{+00}$
78.00	$-7.92 \times 10^{+04}$	$1.34 \times 10^{+03}$	$-4.12 \times 10^{+00}$	$0.00 \times 10^{+00}$
79.00	$-1.67 \times 10^{+05}$	$4.11 \times 10^{+03}$	$-3.33 \times 10^{+01}$	1.02×10^{-01}
80.00	$-1.56 \times 10^{+05}$	$3.69 \times 10^{+03}$	$-2.87 \times 10^{+01}$	8.54×10^{-02}
81.00	$-2.12 \times 10^{+05}$	$5.44 \times 10^{+03}$	$-4.68 \times 10^{+01}$	1.47×10^{-01}
82.00	$-8.26 \times 10^{+04}$	$1.37 \times 10^{+03}$	$-4.37 \times 10^{+00}$	$0.00 \times 10^{+00}$
83.00	$-7.08 \times 10^{+04}$	$1.10 \times 10^{+03}$	$-2.86 \times 10^{+00}$	$0.00 \times 10^{+00}$
84.00	$-7.87 \times 10^{+04}$	$1.24 \times 10^{+03}$	$-3.58 \times 10^{+00}$	$0.00 \times 10^{+00}$
85.00	$-2.97 \times 10^{+05}$	$7.88 \times 10^{+03}$	$-7.08 \times 10^{+01}$	2.26×10^{-01}
86.00	$-7.88 \times 10^{+04}$	$1.23 \times 10^{+03}$	$-3.57 \times 10^{+00}$	$0.00 \times 10^{+00}$
87.00	$-7.69 \times 10^{+04}$	$1.17 \times 10^{+03}$	$-3.27 \times 10^{+00}$	$0.00 \times 10^{+00}$
88.00	$-8.16 \times 10^{+04}$	$1.25 \times 10^{+03}$	$-3.59 \times 10^{+00}$	$0.00 \times 10^{+00}$
89.00	$-8.65 \times 10^{+04}$	$1.34 \times 10^{+03}$	$-4.04 \times 10^{+00}$	$0.00 \times 10^{+00}$
90.00	$-4.27 \times 10^{+05}$	$1.14 \times 10^{+04}$	$-1.04 \times 10^{+02}$	3.27×10^{-01}
91.00	$-5.90 \times 10^{+05}$	$1.63 \times 10^{+04}$	$-1.53 \times 10^{+02}$	4.91×10^{-01}
92.00	$-4.52 \times 10^{+04}$	$5.00 \times 10^{+02}$	$0.00 \times 10^{+00}$	$0.00 \times 10^{+00}$
93.00	$-4.56 \times 10^{+04}$	$4.97 \times 10^{+02}$	$0.00 \times 10^{+00}$	$0.00 \times 10^{+00}$
94.00	$-4.54 \times 10^{+04}$	$4.89 \times 10^{+02}$	$0.00 \times 10^{+00}$	$0.00 \times 10^{+00}$
95.00	$-7.41 \times 10^{+05}$	$2.01 \times 10^{+04}$	$-1.84 \times 10^{+02}$	5.73×10^{-01}
96.00	$-1.31 \times 10^{+06}$	$3.67 \times 10^{+04}$	$-3.46 \times 10^{+02}$	$1.10 \times 10^{+00}$
97.00	$-4.70 \times 10^{+04}$	$4.90 \times 10^{+02}$	$0.00 \times 10^{+00}$	$0.00 \times 10^{+00}$
98.00	$-4.85 \times 10^{+04}$	$5.00 \times 10^{+02}$	$0.00 \times 10^{+00}$	$0.00 \times 10^{+00}$
99.00	$-2.61 \times 10^{+06}$	$7.30 \times 10^{+04}$	$-6.86 \times 10^{+02}$	$2.16 \times 10^{+00}$
100.00	$-1.57 \times 10^{+05}$	$2.53 \times 10^{+03}$	$-9.54 \times 10^{+00}$	6.79×10^{-12}
101.00	$-5.34 \times 10^{+06}$	$1.49 \times 10^{+05}$	$-1.40 \times 10^{+03}$	$4.36 \times 10^{+00}$
102.00	$-1.23 \times 10^{+07}$	$3.46 \times 10^{+05}$	$-3.24 \times 10^{+03}$	$1.01 \times 10^{+01}$
103.00	$-1.40 \times 10^{+07}$	$3.93 \times 10^{+05}$	$-3.66 \times 10^{+03}$	$1.14 \times 10^{+01}$
104.00	$-1.72 \times 10^{+07}$	$4.78 \times 10^{+05}$	$-4.44 \times 10^{+03}$	$1.37 \times 10^{+01}$
105.00	$-5.86 \times 10^{+04}$	$5.58 \times 10^{+02}$	-2.51×10^{-12}	$0.00 \times 10^{+00}$
106.00	$-4.99 \times 10^{+07}$	$1.38 \times 10^{+06}$	$-1.27 \times 10^{+04}$	$3.89 \times 10^{+01}$
107.00	$-2.23 \times 10^{+06}$	$4.05 \times 10^{+04}$	$-1.84 \times 10^{+02}$	$0.00 \times 10^{+00}$
108.00	$-7.35 \times 10^{+04}$	$6.81 \times 10^{+02}$	$0.00 \times 10^{+00}$	$0.00 \times 10^{+00}$
109.00	$4.50 \times 10^{+02}$	$0.00 \times 10^{+00}$	$0.00 \times 10^{+00}$	$0.00 \times 10^{+00}$

[1]C. S. Chen, K. Doi, C. Vyborny, H. P. Chan, and G. Holje, "Monte Carlo simulation studies of detectors used in the measurement of diagnostic x-ray spectra," Med. Phys. **7**, 627–635 (1980).

[2]R. Fahrig and M. J. Yaffe, "A model for optimization of spectral shape in digital mammography," Med. Phys. **21**, 1463–1471 (1994).

[3]M. Hupfer, T. Nowak, R. Brauweiler, F. Eisa, and W. A. Kalender, "Spectral optimization for micro-CT," Med. Phys. **39**, 3229–3239 (2012).

[4]W. A. Kalender, P. Deak, M. Kellermeier, M. van Straten, and S. V. Vollmar, "Application- and patient size-dependent optimization of x-ray spectra for CT," Med. Phys. **36**, 993–1007 (2009).

[5]S. Richard, J. H. Siewerdsen, D. A. Jaffray, D. J. Moseley, and B. Bakhtiar, "Generalized DQE analysis of radiographic and dual-energy imaging using flat-panel detectors," Med. Phys. **32**, 1397–1413 (2005).

[6]M. Weigel, S. V. Vollmar, and W. A. Kalender, "Spectral optimization for dedicated breast CT," Med. Phys. **38**, 114–124 (2011).

[7]B. R. Archer, T. R. Fewell, and L. K. Wagner, "Laplace reconstruction of experimental diagnostic x-ray spectra," Med. Phys. **15**, 832–837 (1988).

[8]B. W. Soole, "A method of X-ray attenuation analysis for approximating the intensity distribution at its point of origin of bremsstrahlung excited in a thick target by incident electrons of constant medium energy," Phys. Med. Biol. **21**, 369–389 (1976).

[9]E. Y. Sidky, L. Yu, X. Pan, Y. Zou, and M. Vannier, "A robust method of x-ray source spectrum estimation from transmission measurements: Demonstrated on computer simulated, scatter-free transmission data," J. Appl. Phys. **97**, 124701–124711 (2005).
[10]Y. Yang, X. Mou, and X. Chen, "A robust x-ray tube spectra measuring method by attenuation data," Proc. SPIE **6142**, 61423K (2006).
[11]J. M. Boone, T. R. Fewell, and R. J. Jennings, "Molybdenum, rhodium, and tungsten anode spectral models using interpolating polynomials with application to mammography," Med. Phys. **24**, 1863–1874 (1997).
[12]J. M. Boone and J. A. Seibert, "Accurate method for computer-generating tungsten anode x-ray spectra from 30 to 140 kV," Med. Phys. **24**, 1661–1670 (1997).
[13]H. A. Kramers, "XCIII. On the theory of X-ray absorption and of the continuous X-ray spectrum," Philosophical Magazine Series 6 **46**, 836–871 (1923).
[14]R. Birch and M. Marshall, "Computation of bremsstrahlung X-ray spectra and comparison with spectra measured with a Ge(Li) detector," Phys. Med. Biol. **24**, 505–517 (1979).
[15]D. M. Tucker, G. T. Barnes, and D. P. Chakraborty, "Semiempirical model for generating tungsten target x-ray spectra," Med. Phys. **18**, 211–218 (1991).
[16]D. M. Tucker, G. T. Barnes, and X. Z. Wu, "Molybdenum target x-ray spectra: A semiempirical model," Med. Phys. **18**, 402–407 (1991).
[17]G. G. Poludniowski and P. M. Evans, "Calculation of x-ray spectra emerging from an x-ray tube. Part I. electron penetration characteristics in x-ray targets," Med. Phys. **34**, 2164–2174 (2007).
[18]M. R. Ay, M. Shahriari, S. Sarkar, M. Adib, and H. Zaidi, "Monte Carlo simulation of x-ray spectra in diagnostic radiology and mammography using MCNP4C," Phys. Med. Biol. **49**, 4897–4917 (2004).
[19]M. Bhat, J. Pattison, G. Bibbo, and M. Caon, "Off-axis x-ray spectra: A comparison of Monte Carlo simulated and computed x-ray spectra with measured spectra," Med. Phys. **26**, 303–309 (1999).
[20]R. E. Alvarez, "Estimator for photon counting energy selective x-ray imaging with multibin pulse height analysis," Med. Phys. **38**, 2324–2334 (2011).
[21]H. Ding and S. Molloi, "Image-based spectral distortion correction for photon-counting x-ray detectors," Med. Phys. **39**, 1864–1876 (2012).
[22]S. Y. Huang, K. Yang, C. K. Abbey, and J. M. Boone, "A semiempirical linear model of indirect, flat-panel x-ray detectors," Med. Phys. **39**, 2108–2118 (2012).
[23]A. Sisniega, W. Zbijewski, A. Badal, I. S. Kyprianou, J. W. Stayman, J. J. Vaquero, and J. H. Siewerdsen, "Monte Carlo study of the effects of system geometry and antiscatter grids on cone-beam CT scatter distributions," Med. Phys. **40**, 051915 (19pp.) (2013).
[24]W. Zbijewski, P. De Jean, P. Prakash, Y. Ding, J. W. Stayman, N. Packard, R. Senn, D. Yang, J. Yorkston, A. Machado, J. A. Carrino, and J. H. Siewerdsen, "A dedicated cone-beam CT system for musculoskeletal extremities imaging: Design, optimization, and initial performance characterization," Med. Phys. **38**, 4700–4713 (2011).
[25]W. Zbijewski, A. Sisniega, J. J. Vaquero, A. Muhit, N. Packard, R. Senn, D. Yang, J. Yorkston, J. A. Carrino, and J. H. Siewerdsen, "Dose and scatter characteristics of a novel cone beam CT system for musculoskeletal extremities," Proc. SPIE **8313**, 831318 (2012).
[26]J. H. Siewerdsen, A. M. Waese, D. J. Moseley, S. Richard, and D. A. Jaffray, "Spektr: A computational tool for x-ray spectral analysis and imaging system optimization," Med. Phys. **31**, 3057–3067 (2004).
[27]T. R. Fewell, R. E. Shuping, and K. E. Healy, *Handbook of Computed Tomography X-ray Spectra*, HHS Publication (FDA) 81-8162 (1981).
[28]J. J. Vaquero, S. Redondo, E. Lage, M. Abella, A. Sisniega, G. Tapias, M. L. S. Montenegro, and M. Desco, "Assessment of a new high-performance small-animal X-ray tomograph," IEEE Trans. Nucl. Sci. **55**, 898–905 (2008).
[29]K. Meghzifene, H. Aiginger, and R. Nowotny, "A fit method for the determination of inherent filtration with diagnostic x-ray units," Phys. Med. Biol. **51**, 2585–2597 (2006).
[30]H. E. Johns and J. R. Cunningham, *The Physics of Radiology* (Charles C. Thomas, Springfield, IL, 1983).
[31]R. Nowotny and K. Meghzifene, "Simulation of the effect of anode surface roughness on diagnostic x-ray spectra," Phys. Med. Biol. **47**, 3973–3983 (2002).
[32]M. R. Ay, S. Sarkar, M. Shahriari, D. Sardari, and H. Zaidi, "Assessment of different computational models for generation of x-ray spectra in diagnostic radiology and mammography," Med. Phys. **32**, 1660–1675 (2005).
[33]R. Birch, M. Marshall, and G. M. Ardran, *Catalogue of Spectral Data for Diagnostic X-rays* (Hospital Physicists' Association, London, 1979).
[34]S. H. Heo, A. Ihsan, and S. O. Cho, "Transmission-type microfocus x-ray tube using carbon nanotube field emitters," Appl. Phys. Lett. **90**, 183109 (2007).
[35]D. H. Larsson, U. Lundström, U. K. Westermark, M. Arsenian Henriksson, A. Burvall, and H. M. Hertz, "First application of liquid-metal-jet sources for small-animal imaging: High-resolution CT and phase-contrast tumor demarcation," Med. Phys. **40**, 021909 (7pp.) (2013).